A study of weldability and fracture modes in electron beam weldments of AZ series magnesium alloys

Chao-Ting Chi [a,b,*], Chuen-Guang Chao [a], Tzeng-Feng Liu [a], Che-Chung Wang [c]

[a] *Department of Materials Science and Engineering, National Chiao Tung University, Hsinchu 300, Taiwan, ROC*
[b] *System Manufacturing Center, Chung-Shan Institute of Science and Technology, PO Box 90008-14, Sanxia 237, Taipei, Taiwan, ROC*
[c] *Graduate School of Industrial Design and Architecture, Shih-Chien University, Taipei 104, Taiwan, ROC*

Abstract

Given the growing need for environmental protection and lightweight construction, electron beam welding (EBW) is becoming the most important welding technology because it can compensate for the poor formability of magnesium alloys. This paper examines interactions between the properties of three AZ series magnesium alloys and welding conditions. The EBW process can yield four kinds of defect in a weld: cavities, the heat-affected zone (HAZ), undercuts, and root concavities. These defects obviously induce stress concentrations in the weld, and may seriously damage its strength. Additionally, the distribution of precipitates (γ phase, $Mg_{17}Al_{12}$) in the fusion zone (FZ) changes from a relatively small number of scattered particles to a dense population of dendrites as the Al content of the magnesium alloy increases. Under excessive tensile stress, alloy weldments break in one of two fracture modes: an irregular FZ fracture, or a regular HAZ fracture. AZ31B usually exhibits the former mode and AZ91D the latter, while AZ61A exhibits each mode half the time. The overall weldability, which depends on the random distribution of these precipitates and defects, is found to be greatest for the AZ61A alloy. The best process window, on the other hand, is found for the AZ91D alloy. Finally, we obtain optimum parameters for the EBW process and empirical formulae for the weldment strength as a function of these parameters. These results are closely related to each other.

1. Introduction

Recent years have witnessed the increased use of magnesium alloys in the aerospace, transportation, national defense and 3C industries, both to protect the environment and meet the requirements of lightweight designs. AZ series alloys have dominated other magnesium alloys in die casting applications [1] whose product performances can be improved further by a forging process. Magnesium alloys have poor formability and high reactivity, however, which limits their modes of manufacture. Ideally, the production of a complex assembly in magnesium alloy can be accomplished by combining simple forging parts under appropriate welding conditions. This approach has been shown to achieve performance standards comparable to those obtained by the single-step processes used for other structural materials.

Because of their low melting point, high chemical activity, and high thermal conduction, magnesium alloys must be welded at high power under a flux or vacuum environment. Hence, the strength of a weldment is much lower than that of the base material. Not only are the grains coarsened, but many cavities and cracks formed in FZ and HAZ [2,3]. The industrial application of traditional welding methods has mainly been limited to arc and solid state welding [4–6]. The characteristics of high energy density beam welding (HBW) can eliminate the aforementioned shortcomings, therefore this approach is gradually becoming the principal technology used in joining magnesium alloys. Numerous works on the HBW of magnesium alloys have concentrated their discussion on laser welding [7–9]. Although laser welding is a very convenient method, its energy limitations restrict the degree of fusion penetration in thicker work

* Corresponding author at: Department of Materials Science and Engineering, National Chiao Tung University, Hsinchu 300, Taiwan, ROC.
Tel.: +886 916 930630.
E-mail addresses: joseph.mse92g@nctu.edu.tw (C.-T. Chi),
c_g_chao@hotmail.com (C.-G. Chao), coe@cc.nctu.edu.tw (T.-F. Liu),
zcwang@mail.usc.edu.tw (C.-C. Wang).

pieces [10]. It is for this reason that EBW is the preferable choice.

EBW technology can maximize both the precision and the depth-to-width ratio of the weld. Since its creation in the 1950s, this method has been at the forefront of the welding field [11]. Following an extensive period of research and development, a major breakthrough in the technology was made at the beginning of the 21th century: in 2001, Banhart used EBW to solder carbon nanotubes of 15 nm diameter [12]. Banhart was the first to accomplish such a feat, and his work opened up a new era of welding technology. The results of this work have significantly influenced future practical applications of EBW.

Five factors control the EBW process and affect the quality of the weld, including accelerating voltage (V, kV), beam current (I, mA), welding speed (υ, mm/s), vacuum level (below 10^{-3} Torr), and the spot size (φ, mm) of the electron beam on the surface of the work piece [13]. The EBW equipment is commonly operated in a high vacuum [14], so the loss of electron energy due to scattering is very small. Accordingly, the input energy (E, J) of EBW can be expressed as [15]:

$$E = \frac{\eta}{4.2} \frac{VI\varphi}{\upsilon} = \frac{\eta}{4.2} \frac{P\varphi}{\upsilon} \qquad (1.1)$$

where η is the transfer efficiency and P is the total output power (W) of the electron beam.

The transfer efficiency of EBW energy, while generally the highest among all welding technologies, is still not 100% because some of the input energy goes to heating material in the zone adjacent to the weld and overheating and evaporating liquid metal in the FZ. Whether or not the weldment undergoes complete fusion penetration will therefore depend on the thermal transfer efficiency (η_t) of the EBW [16–18]:

$$\eta_t = \frac{P_f}{P_e} = \frac{\upsilon A H}{P_e} \qquad (1.2)$$

$$P_e = P\eta_e \qquad (1.3)$$

$$H = C(T_m - T_0) + H_f \qquad (1.4)$$

In the above formulae, η_e is a coefficient taking into account the energy dissipated by backscattered electrons, P_f the effective beam power, P_e the input power, A the cross-sectional area of the melting zone, H the heat content, C the mean specific heat from room temperature to melting temperature (T_0, T_m), and H_f is the heat of fusion.

When magnesium alloys are joined by EBW, equiaxial grains with small diameters are created inside the FZ (which has no columnar grain) due to the high cooling rate. Because melting magnesium alloys have a higher vapor pressure and greater fluidity than other structural materials, the weld surface destabilizes easily. The grain size of the weld and the evaporation of the magnesium alloy can both be decreased by raising the welding speed, but this also causes many cavities to form in the weld root and an uneven appearance on the weld surface. At this time, certain operating practices such as reducing the welding speed and using a slightly defocused beam can help to create sound welds [2]. When the Al content of a magnesium alloy is slightly increased, not only does the depth of the weld

increase but the weld surface becomes smoother. Ripples and spatters also become less distinct in such alloys [19]. In contrast, a high Zn content (above 1%) or excessive welding energy increases the vapor pressure and decreases the weld quality [2]. The above facts demonstrate that the process window (or parameter window) of magnesium alloys might be narrower than that of other engineering materials [20]. Imperfections in the functional parameters [13] and the addition of unsuitable elements caused defects in the FZ can markedly affect the quality of the resulting weld.

Magnesium alloys and EBW equipment are expensive, so only a few articles have been published on the use of EBW on Mg alloys [17,19–21]. To date, only one paper has systematically researched control parameters [22]. This subject should therefore be studied more closely. Preceding studies have left unanswered many questions regarding the weldability, process window, optimum parameters, types of defect, empirical strength formulas, and weldment fracture modes of EBW of magnesium alloys. This study will clarify all these topics.

2. Experimental method

Homemade AZ31B, AZ61A, and AZ91D extrusive plates with dimensions of 105 mm × 60 mm × 12 mm were used in this study. A layer 0.5 mm thick was removed from the surface of these plates around the welding area, to prevent the oxide layer from having any effect on the results. As displayed in Fig. 1(a), two plates were welded together by an autogenous butt joint process. The dimensions of the resulting structure were thus 105 mm × 120 mm × 11 mm. In a vacuum (3×10^{-5} Torr) environment, the variable parameters of EBW were chosen to yield five fixed power values (3000, 3500, 4000, 4500 and 5000 W). There were three controlled parameters in this process: the beam current (60–167 mA), the accelerating voltage (20–50 kV), and the welding speed (60.6, 73.3, or 86.0 mm/s). The focal position was at the bottom of the work piece. Only one parameter was varied at a time, and a total of 75 pairs of specimens were welded under various conditions.

As presented in Fig. 1(a)–(c), these weldments were cut into one metallographic and six tensile specimens along the direction of extrusion. The EBW channel was halfway along the length of the gauge in the standard tensile specimens, perpendicular to the longitudinal direction. The properties of all weldments were measured for at least three specimens, so that tensile tests can report the average ultimate tensile strength (UTS) and estimate the difference between the optimal and worst weldments. After the fractured sample and metallographic specimen were cut and cleaned as shown in Fig. 1(d), they were analyzed using a scanning electron microscope (SEM), an energy dispersive spectrometer (EDS), and an electron probe X-ray micro-analyzer (EPMA) to elucidate the reasons for each fracture. Moreover, except the microstructure of the weld boundary was observed, as indicated in Fig. 1(e), the metallographic specimens were divided into two pieces along the central line of the weld cross-section. The preferred orientation and specific phase of weldments could be identified by using X-ray diffraction (XRD).
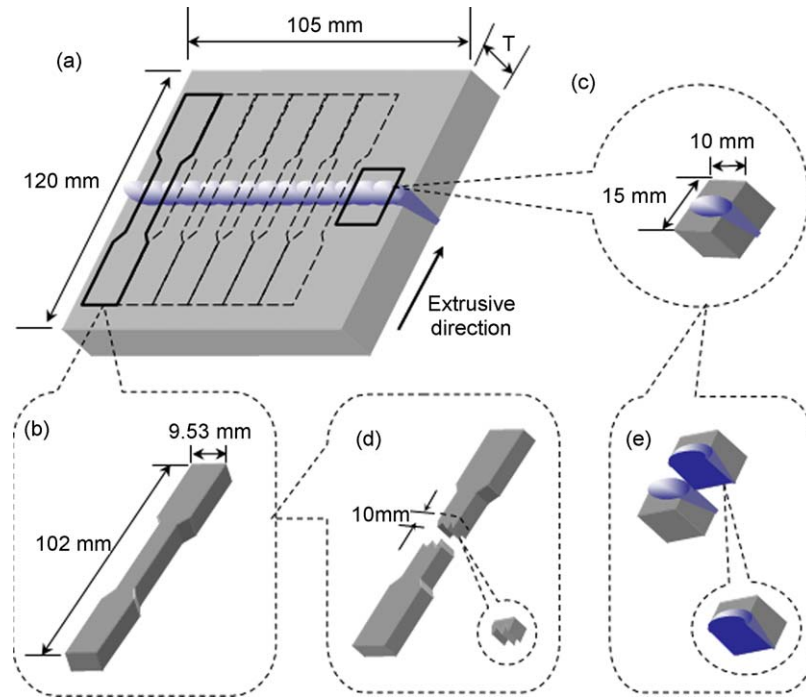
Fig. 1. Preparation of the magnesium alloy samples by EBW for various inspection purposes.

3. Results and discussion

3.1. Analysis of chemical composition

The chemical compositions of magnesium alloys AZ31B, AZ61A and AZ91D were analyzed using an inductively coupled plasma-atom emission spectrometer and mass spectrometer (ICP-AES and ICP-MS). As Table 1 shows, all of the chemical constituents satisfy ASTM standards.

3.2. Tensile test

In this study, 75 sets of work pieces were welded for each magnesium alloy to explore a wide range of control parameters. All the work pieces with complete fusion penetration were compared in a tensile test to measure their UTS, and the welding conditions of the base material were recorded for the group's optimum and worst weldments. As shown in Table 2, the UTS of magnesium alloys in the AZ series increases with Al content.

Table 1
Chemical composition for AZ series magnesium alloys (wt.%)

Materials	Element				
	Mg (Cu)	Al (Fe)	Zn (P)	Mn (Pb)	Si (Be)
AZ31B	96.2467 (0.0004)	2.8150 (0.0025)	0.6395 (0.0013)	0.2835 (0.0008)	0.0094 (0.0009)
AZ61A	93.0585 (0.0007)	5.8800 (0.0030)	0.7985 (0.0012)	0.2205 (0.0062)	0.0240 (–)
AZ91D	90.3148 (0.0012)	8.8550 (0.0041)	0.5474 (0.0012)	0.2600 (0.0017)	0.0143 (0.0003)

Table 2
A comparison of UTS, strain, and control parameters among the three AZ series magnesium alloys and their optimum and worst weldments

Material (matrix strength, strain rate)	Item		
	State	Weldment strength (strain rate)	Welding parameters
AZ31B (296.9 MPa, 29.9%)	Optimum	234.1 MPa (2.6%)	50 kV/100 mA/60.6 mm/s
	Worst	151.3 MPa (1.3%)	45 kV/100 mA/86.0 mm/s
AZ61A (297.4 MPa, 28.1%)	Optimum	247.5 MPa (7.4%)	50 kV/100 mA/60.6 mm/s
	Worst	168.1 MPa (1.8%)	45 kV/100 mA/86.0 mm/s
AZ91D (323.3 MPa, 22.9%)	Optimum	266.0 MPa (5.9%)	40 kV/113 mA/73.3 mm/s
	Worst	175.7 MPa (1.6%)	45 kV/100 mA/86.0 mm/s

Note: Focal positions are at the bottom of work piece for all samples. The strength reported here is the ultimate tensile strength (UTS).

Even when these specimens were welded with identical control parameters (as was the case for the worst weldments of all three alloys), the same trends are followed. Relative to the alloy matrix strength, we obtain UTS values of 78.8%, 83.2%, and 82.2% for the optimum weldments of AZ31B, AZ61A, and AZ91D, respectively. Likewise, the optimum weldment/base material strain ratios for these alloys are 8.7%, 26.3%, and 25.8%. These results indicate that in order of decreasing weldability, the three materials may be ranked AZ61A, AZ91D, and AZ31B.

Fig. 2 plots stress-strain curves for the base material, the optimum weld, and the worst weld for the alloys AZ31B, AZ61A and AZ91D. First, comparing the curves of the AZ series base materials demonstrates that AZ31B has the highest yield strength; exhibits necking during tensile testing. In contrast, AZ61A and AZ91D have UTS values equal to their fracture strength and exhibit no necking. Thus, it is clear that the UTS increases and the ductility decreases with increasing Al content in these alloys. Next, relative to the alloy matrix strength, we obtain UTS values of 50.9%, 56.5%, and 54.3% for the worst weldments of AZ31B, AZ61A, and AZ91D, respectively. Likewise, the worst weldment/base material strain ratios for these alloys are 4.3%, 6.4% and 7.0%. Although the strain ratio of the worst AZ91D weldment slightly exceeds that of the worst AZ61A weldment, the latter clearly reaches the highest UTS value. Hence, even in the worst case the weldability of these materials remains in the order AZ61A, AZ91D, and AZ31B.

The process window (or parameter window) is an index describing the ease of meeting process requirements, and can be estimated by a method similar to that used to evaluate the weldability. In this study, the distribution of UTS ratios (weldment/base material) for all 75 weldments of each alloy, as presented in Fig. 3, can be used to determine the process window. At welding powers below 4000 W, joint penetration is incomplete in all cases except for a few AZ61A and AZ91D weldments. Notably, the peak of the UTS distribution lies between 60% and 70% for AZ61A, and between 70% and 80% for AZ91D. The UTS distribution for AZ31B weldments, on the other hand, is
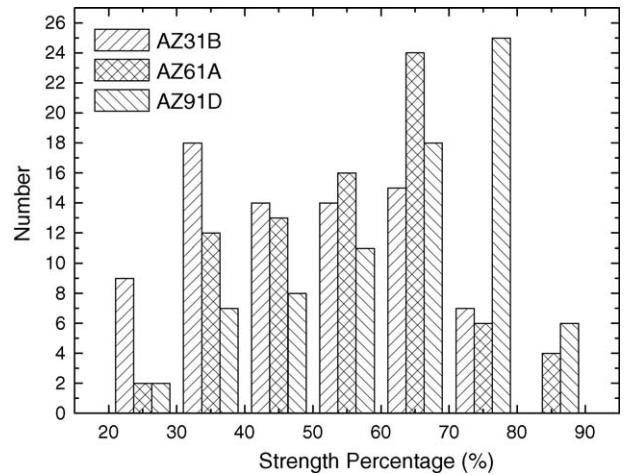

Fig. 3. Distribution of UTS ratios for all weldments in the AZ series of magnesium alloys.

approximately uniform over the range 30–70%. Furthermore, the number of weldments with a UTS ratio between 80% and 90% is only zero, four, and six for the AZ31B, AZ61A, and AZ91D alloys, respectively. All these data indicate that AZ91D has the best EBW process window of all three alloys, followed by AZ61A and then AZ31B.

The 75 UTS data points for each magnesium alloy were analyzed using nonlinear regression (we used the statistical software STATISTICA), and their regression curves are plotted in Figs. 4–6. The analysis imposes a maximum power of 5000 W, and only considers UTS values lower than the base material's practical maximum. The R^2 statistic gives the probability that the predicted and experimental values are linearly correlated. The empirical formula used to predict the UTS is

$$\text{UTS} = K \frac{V^a I^b}{v^c} \tag{3.1}$$

where K is the transfer coefficient. Table 3 presents the best-fit values of a, b, and c. The bands drawn in Figs. 4–6 (dashed lines) represent a confidence level of 95%. The electron beam current was measured in the generating assembly of the EBW equipment, so the total output power of the electron beam could be obtained directly. Based on formulae (1.1)–(1.4), the total
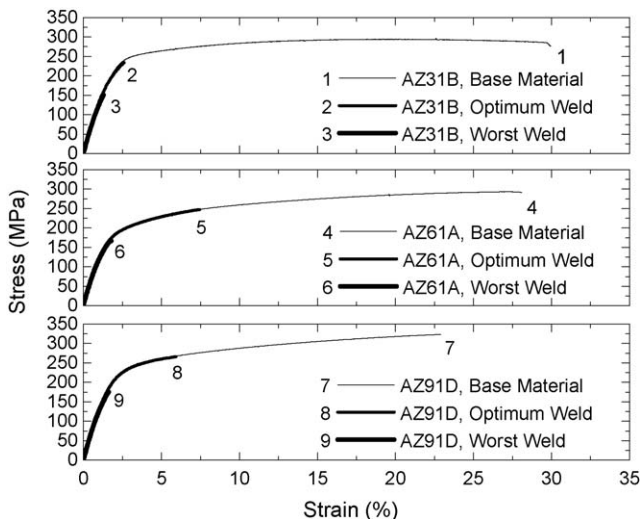

Fig. 2. Stress–strain curves for the base materials, the optimum weld, and the worst weld in AZ alloys. (Table 2 gives the welding parameters of each sample.)
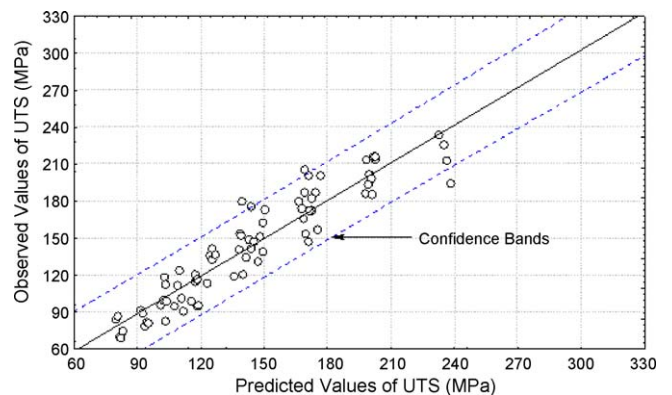

Fig. 4. UTS errors in a nonlinear regression analysis of AZ31B.
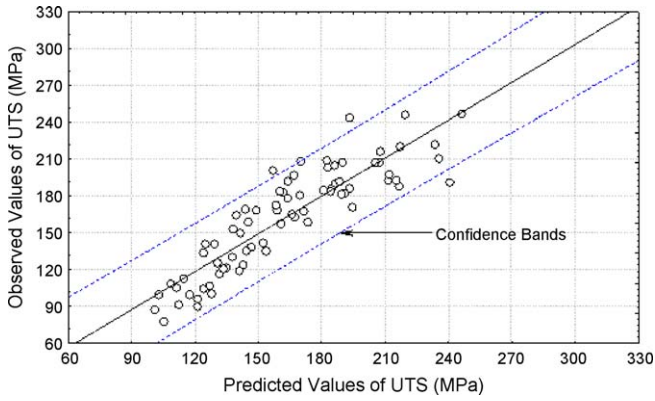
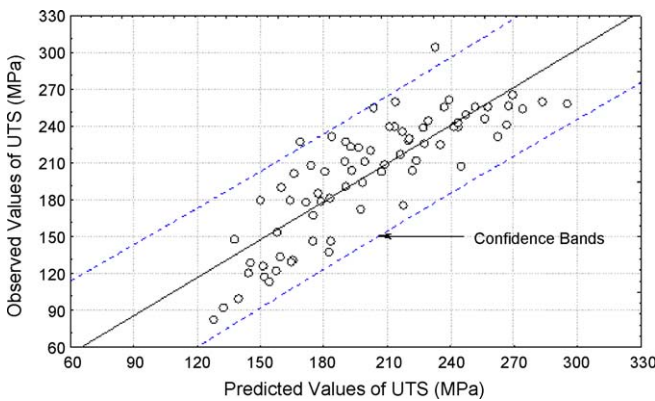Fig. 5. UTS errors in a nonlinear regression analysis of AZ61A.

Fig. 6. UTS errors in a nonlinear regression analysis of AZ91D.

Table 3
Best-fit UTS formula parameters from a nonlinear regression analysis

AZ alloys	Coefficients				R^2
	K	a	b	c	
AZ31B	0.024	1.466	1.507	0.854	0.938
AZ61A	0.238	1.199	1.092	0.676	0.889
AZ91D	0.414	1.127	0.944	0.533	0.836

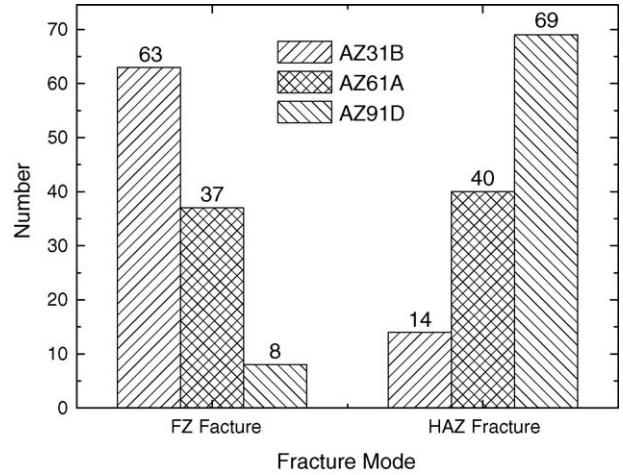Nonlinear model equation: UTS $= KV^a I^b / \upsilon^c$.

Fig. 8. Histogram of weld fracture modes in the AZ series of magnesium alloys.

efficiency of EBW and an estimate of K can be derived as follows

$$\eta = \eta_t \eta_e = \frac{P_f}{P} \tag{3.2}$$

$$K \approx \eta \varphi \tag{3.3}$$

Eq. (3.3) relates the transfer coefficient K to the transfer efficiency η and the spot size φ of EBW. It is therefore clear that there must be a close relationship between UTS and η. The UTS of a weldment has been found to increase continuously as the focal position moves from the surface to the bottom of a work piece [22]; that is to say, the UTS of a weldment is directly proportional to the spot size of the electron beam. Eq. (3.1) can therefore be very useful in determining practical EBW operating parameters for alloys in the AZ-series.

Visual observations reveal that the fracture surfaces of all weldment tensile samples can be divided into two modes: an irregular FZ fracture, as shown in Fig. 7(a), and a regular HAZ fracture, as shown in Fig. 7(b). In the former mode, cracks running randomly across the middle of the weld are initiated and terminated in an undercut, HAZ, or root concavity; in the latter, a break occurs along the weld boundary. The histograms in Fig. 8 show that 80.8% of the AZ31B weldments and 11.5% of
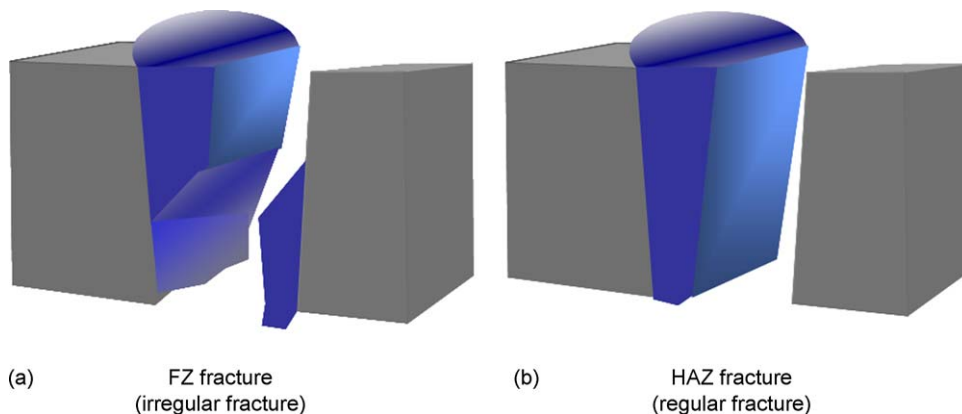

Fig. 7. Schematic of EBW fracture modes in the AZ series of magnesium alloys.

the AZ91D weldments exhibited FZ fractures. In contrast, the two fracture modes were almost equally likely in the AZ61A weldments, with 48% exhibiting FZ fractures and 52% exhibiting HAZ fractures. These results suggest that microstructural changes in the weld influence the initiation and propagation of cracks in the AZ series alloys. More precisely, the phase composition of the microstructure may be closely related to the elemental Al content.

3.3. Microstructure observations

Direct observation of microstructure is the most important method of determining the fracture mode. Fig. 9 displays cross-sectional metallographs of the optimum (Fig. 9(a)–(c)) and worst (Fig. 9(d)–(f)) welds in all three alloys. Cavities (arrows), under-cuts (circles), and root concavities (ellipses) are all fatal factors that can cause excessive stress concentrations in a poor weld, and reduce the UTS of the weldment.

Fig. 10(a)–(c) shows SEM photographs of the optimal weld boundaries, magnifying the rectangular regions indicated in Fig. 9(a)–(c). Many precipitates concentrate in the FZ, in a distribution that tends to grow from a few scattered particles to densely packed dendrites as the Al content increases. An EDS analysis, as displayed in the lower left corners of Fig. 10(a)–(c), reveals that the precipitates have a higher Al and Zn content than the vicinal matrix. Furthermore, EPMA analysis yields a
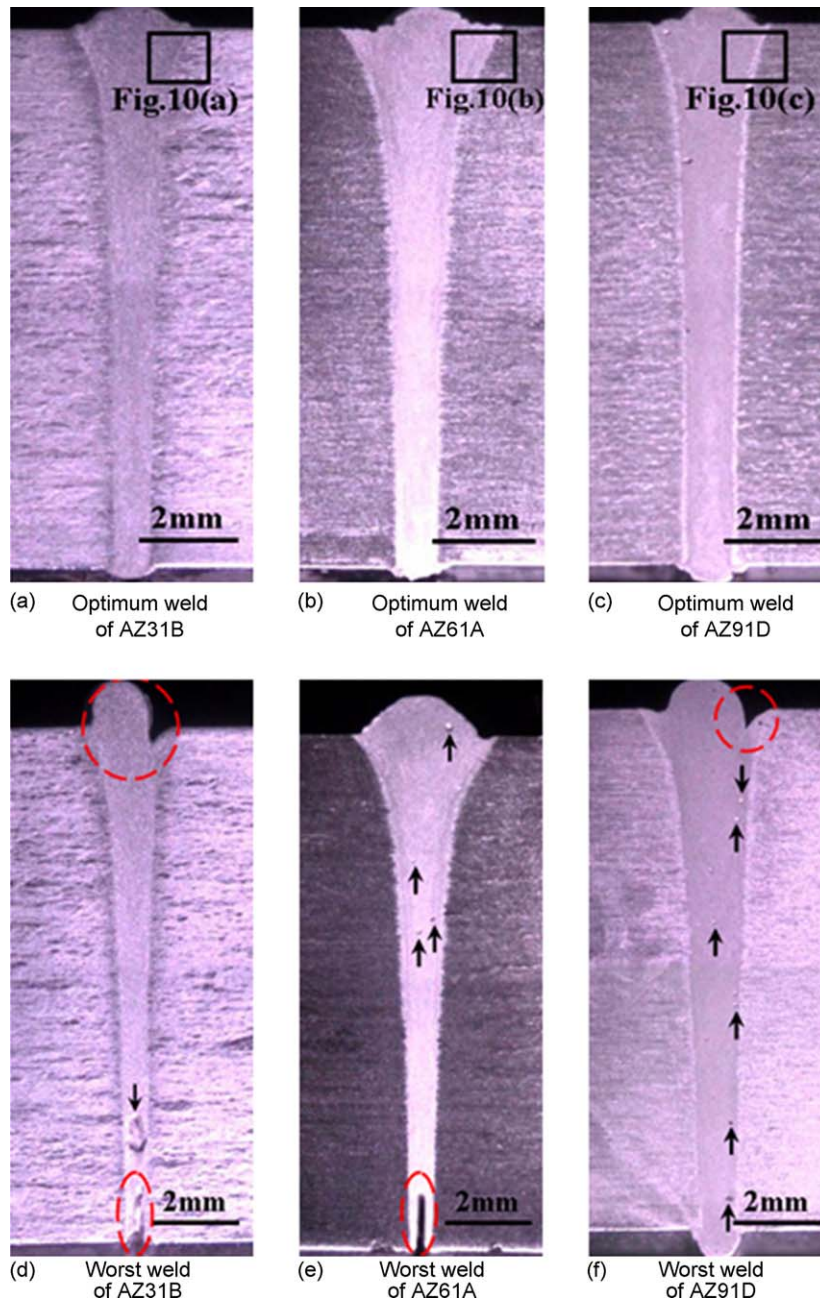

Fig. 9. Cross-sectional metallographs of the optimum and worst welds of all three AZ series alloys. (Table 2 presents the parametric conditions of each sample.)
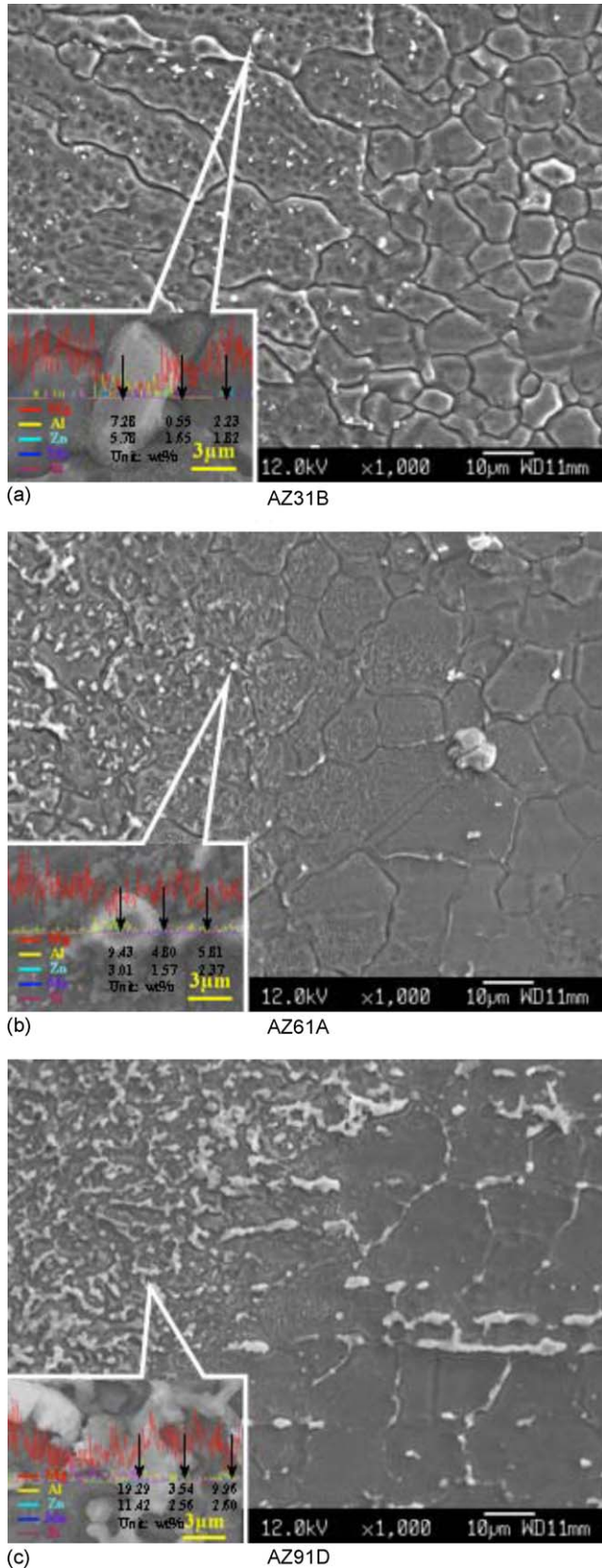
line scan curves across the top, middle, and bottom weld boundaries as presented in Fig. 11. The Mg and Al content (vertical axis) in the FZ fluctuates as expected, since many precipitates form there. The number of such precipitates increases with Al content (Fig. 11(a)–(f)). Additionally, local differences in the input energy and heating time cause the number of precipitates to decrease from the top to the bottom of the FZ (Fig. 11(e)–(j)). Clearly, the distribution of precipitates affects the mechanical properties of the weldments and changes the probable fracture mode.

3.4. XRD analysis

The preferred orientation and special phases of AZ series magnesium alloys can be analyzed by XRD. As shown in Fig. 12(a)–(c), the $(10\bar{1}0)$ plane which lies on the transverse plane of the extruded plate is the preferred orientation of all alloys before EBW. The peak intensity of this direction decreases as the Al content of the alloy increases. After EBW, the forging structure is converted to a casting structure and the original preferred orientation has disappeared in the weld. The preferred orientation of a casting structure, such

Fig. 10. SEM enlargements of the weld boundary regions shown in Fig. 9(a)–(c). (Lower left: an enlargement of the photograph obtained by EDS analysis.)
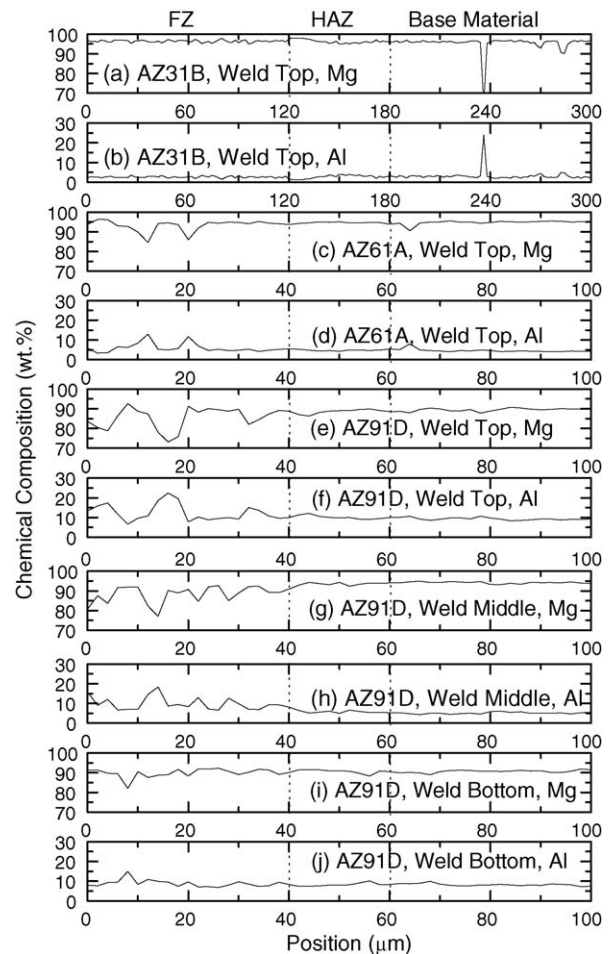

Fig. 11. EPMA analysis of the optimum weld boundaries for each AZ series magnesium alloy. (Table 2 gives the parametric conditions of each sample.)
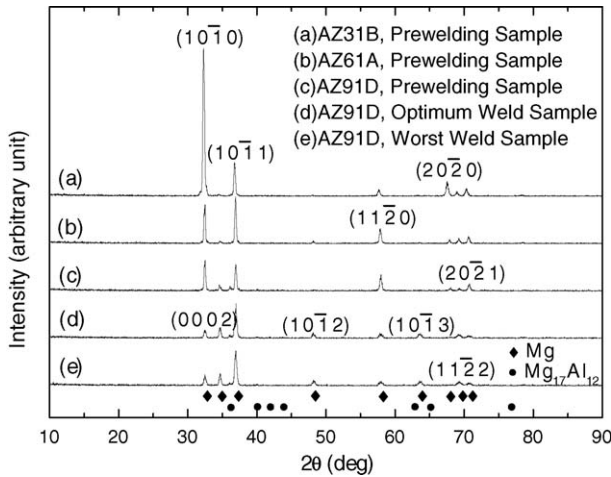
Fig. 12. XRD analysis of weld boundaries for the AZ series magnesium alloys. (Table 2 gives the parametric conditions of each sample.)

as the $(1\,0\,\bar{1}\,0)$ peak seen in Fig. 12(d)–(e) which is not as obvious as that of a forging structure, even though affected slightly by epitaxy growth along the weld boundary. The γ phase is the sole intermetallic compound, but its peak is not well marked either before or after welding for any choice of operating parameters.

The observations described in the last few paragraphs indicate that the distribution of the brittle γ phase changes from scattered particles to dense dendrites as the Al content increases. At the same time, the strength of the FZ increases and the preferred fracture mode changes from FZ to HAZ. The ductility of the optimum weldment does not improve, however,

because only the brittle γ phase forms microstructures in the FZ.

3.5. Microindentation hardness test

Fig. 13(a) and (b) presents the positions and results of microindentation hardness testing on the weld cross-section. Microindentation hardness values for the FZ, HAZ, and base material increase with increasing Al content in the magnesium alloy. The brittle γ phases are found mainly in the center of the upper weld, and their spatial distribution causes the hardness to decrease towards the bottom of the sample and away from the FZ axis. Both the vertical and horizontal test results agree with the curves obtained by EPMA analysis. Moreover, a comparison of the optimum and worst weldments clearly shows that the curve of the former is more symmetrical than that of the latter. This is because an imperfect choice of operating parameters causes cavities in the weld and coarsens the grains, which increases the area of indentation and influences microindentation test results. Hence, at random positions the microindentation hardness of the weld may decline suddenly, for example at the points (−1.5, 5.0), (0.5, 0) and (0, −5.0).

All the observations mentioned above support our previous deductions concerning the nature of the fracture modes. The crack is initiated at an undercut, HAZ, or root concavity, and then propagates either along the HAZ boundary or through the FZ by linking cavities or softening zones. Finally, the probability of FZ and HAZ fractures is determined by the distribution of precipitates with Al content in AZ series magnesium alloys.
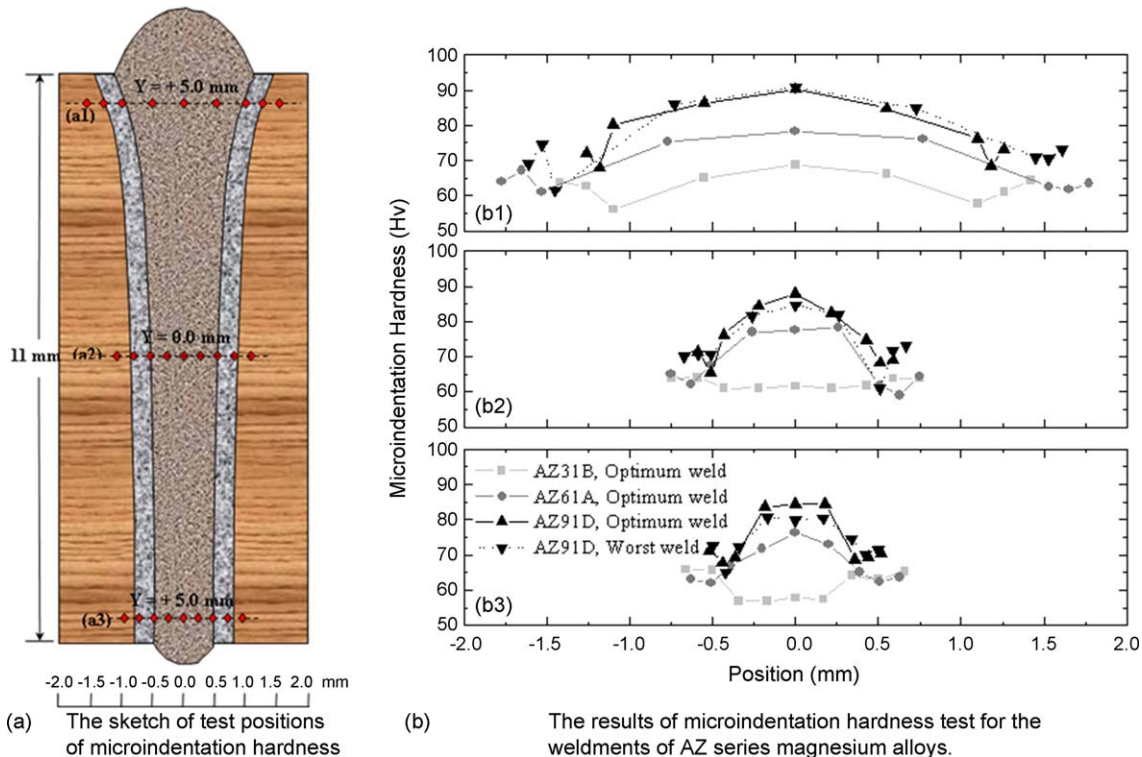

(a) The sketch of test positions of microindentation hardness

(b) The results of microindentation hardness test for the weldments of AZ series magnesium alloys.

Fig. 13. Microindentation hardness testing of the weld cross-section in AZ series magnesium alloys.

4. Conclusions

In summary, increasing the Al content in AZ series magnesium alloys (up to 10%) increases both the strength and microindentation hardness of the weld, and decreases its ductility. This effect is due to the increasing concentration of brittle precipitates (γ phase, $Mg_{17}Al_{12}$) in the FZ, which can take on a variety of forms ranging from scattered particles to densely packed dendrites. Fracturing of the AZ series alloys can occur in one of two modes: an irregular FZ fracture, or a regular HAZ fracture. AZ31B tends to exhibit the former mode, and AZ91D tends to exhibit the latter. AZ61A, on the other hand, exhibits the two fracture modes in equal proportion.

In the AZ series magnesium alloys, defects such as cavities, the HAZ, undercuts, and root concavities can create excessive stress concentrations and reduce the UTS and ductility of a weldment. In terms of their weldability, which is determined by the distribution of precipitates and defects, these alloys can be ranked in decreasing order as AZ61A, AZ91D, and AZ31B. AZ91D has the best process window, on the other hand, followed by AZ61A and then AZ31B. Empirical formulas for the UTS and optimum EBW parameters for each of the AZ series alloys are as follows:

- AZ31B: UTS $= 0.024V^{1.466}I^{1.507}/S^{0.854}$, condition: 50 kV/100 mA/60.6 mm/s/focus at bottom;
- AZ61A: UTS $= 0.238V^{1.199}I^{1.092}/S^{0.676}$, condition: 50 kV/100 mA/60.6 mm/s/focus at bottom;
- AZ91D: UTS $= 0.414V^{1.127}I^{0.944}/S^{0.533}$, condition: 40 kV/113 mA/73.3 mm/s/focus at bottom.

References

[1] I.J. Polmear, Mater. Sci. Technol. 10 (1994) 1–16.
[2] M.M. Avedesian, H. Baker, ASM Specialty Handbook, ASM International, USA, 1999.
[3] M. Rethmeier, S. Wiesner, H. Wohlfahrt, Magnesium Alloys Appl. (2000) 200–204.
[4] U. Draugelates, A. Schram, B. Bouaifi, C. Kettler, Magnesium Alloys Appl. (1998) 29–35.
[5] A. Munitz, C. Cotler, A. Stern, G. Kohn, Mater. Sci. Eng. A 302 (2001) 68–73.
[6] L.M. Liu, G. Song, G.L. Liang, J.F. Wang, Mater. Sci. Eng. A 390 (2005) 76–80.
[7] A. Weisheit, R. Galun, B.L. Mordike, Weld. Res. Suppl. (1998) 149–154.
[8] L.K. Pan, C.C. Wang, Y.C. Hsiao, K.C. Ho, Opt. Laser Technol. 37 (2004) 33–42.
[9] L.K. Pan, C.C. Wang, Y.C. Shin, H.F. Sher, Sci. Technol. Weld. Join. 10 (4) (2005) 1–8.
[10] D.E. Powers, G.R. Laflamme, Weld. J. (1992) 47–52.
[11] Z. Sun, R. Karppi, J. Mater. Process. Technol. 59 (1996) 257–267.
[12] F. Banhart, Nano Lett. 1 (6) (2001) 329–332.
[13] U. Dilthey, J. Weiser, Weld. World 39 (2) (1997) 89–98.
[14] AWS F2.1–78 (1978) 1–8.
[15] T. Hashimoto, F. Matsuda, Trans. Natl. Res. I. Met. 7 (3) (1965) 22–35.
[16] G. Mladenov, K. Vutova, S. Wojcicki, Vacuum 51 (2) (1998) 231–233.
[17] E. Koleva, G. Mladenov, K. Vutova, Vacuum 53 (1) (1999) 67–70.
[18] E. Koleva, Vacuum 77 (2005) 413–421.
[19] S.F. Su, J.C. Huang, H.K. Lin, N.J. Ho, Metall. Mater. Trans. A 33 (5) (2002) 1461–1473.
[20] H. Haferkamp, U. Dilthey, G. Träger, I. Burmester, M. Niemeyer, Magnesium Alloys Appl. (1998) 595–600.
[21] C. Vogelei, D. Dobeneck, I. Decker, H. Wohlfahrt, Magnesium Alloys Appl. (2000) 191–199.
[22] C.T. Chi, C.G. Chao, C.A. Huang, C.H. Lee, Mater. Sci. Forum 505–507 (2006) 193–198.